Journal of Non-Newtonian Fluid Mechanics 196 (2013) 36–50

Contents lists available at SciVerse ScienceDirect

Journal of Non-Newtonian Fluid Mechanics

journal homepage: http://www.elsevier.com/locate/jnnfm

A new twist on Stokes' second problem: Partial penetration of nonlinearity in sheared viscoelastic layers

Paula A. Vasquez [a,*], Yuan Jin [a], Kim Vuong [a], David B. Hill [b], M. Gregory Forest [a]

[a] Department of Mathematics, University of North Carolina, Chapel Hill, NC 27599-3250, United States
[b] Cystic Fibrosis Center, University of North Carolina, Chapel Hill, NC 27599-7248, United States

ARTICLE INFO

Article history:
Received 13 September 2012
Received in revised form 28 December 2012
Accepted 31 December 2012
Available online 22 January 2013

Keywords:
Viscoelastic shear wave
Giesekus model
Stokes' second problem
LAOS
Biological fluids

ABSTRACT

Fully nonlinear flow-constitutive model simulations are employed to investigate constructive and destructive interference of counter-propagating shear waves and their associated stress profiles within a viscoelastic layer of "intermediate depth". Linear unidirectional shear waves in sufficiently thick viscoelastic layers, the viscoelastic analog of Stokes' second problem, were exploited as a rheological tool by Ferry et al. [1,2]. The extension to intermediate gap heights for linear and nonlinear driving amplitudes was studied by our group [3–5], and by Balmforth et al. [6] for viscoplastic fluids. Here we explore the nonlinear quasi-stationary response of the entire viscoelastic layer to an oscillating boundary, greater than the gap-loading limit of typical shear rheometers but less than the depth of effective attenuation. We illustrate how to tune the degree and partitioning of nonlinearity versus driving amplitude and frequency, gap height, and fluid viscoelasticity.

1. Introduction

The motivation for this study arises from laboratory evidence of heterogeneous standing waves induced by coordinated epithelial cilia in lung cell cultures together with the fundamental question of whether mucus transport in the cell culture (and indeed in lung airways) is governed by linear or nonlinear viscoelasticity. Mucus layers line the airways to protect the lungs against inhaled particulates, bacteria, viruses, and other harmful substances. The effectiveness of mucus clearance to rid the lung of airborne matter is based on the interplay between cilia, air drag, mucus, and the periciliary fluid that surrounds the cilia. Both coordinated cilia and phasic air drag continuously provide oscillatory shear driving conditions on the mucus layer. Very little evidence is available on the details of mucus response *in vivo*. In recent years, development of human bronchial epithelial (HBE) cultures [7] has afforded detailed laboratory observations, illustrated in Fig. 1, with coordinated cilia driving the flow. Position time series of passive microbead tracers are captured at several heights between the cilia tips and the air-mucus interface. Oscillatory shear is seen to dominate the mucus flow field, since the neutrally buoyant beads remain at the same height within experimental resolution and duration. Furthermore, the height-dependent bead displacements show a dynamic heterogeneous shear strain characterized by an attenuation in the shear wave amplitude with height above the cilia.

These laboratory observations raise the question as to whether height-dependent bead time series carry information about the viscoelastic properties of the mucus layer; e.g., could the distributed time series data be used to infer linear dynamic moduli as a generalization of the Ferry–Adler–Sawyer [1,2] protocol? Speculating further, is it possible to infer that specific heights exhibit nonlinear response whereas others exhibit linear response, and to infer the nature of that response akin to LAOS in rheometric shear conditions [8–10]?

In this work we extend our previous studies [3–5] of viscoelastic layers under oscillatory driving conditions in a planar shear cell geometry to probe these questions. We use the parallel plate geometry instead of the cell culture or airway geometries because the analysis and simulations reduce to one spatial dimension, a significant reduction in numerical complexity and cost. These conditions require plate gap heights between the gap loading and Ferry–Adler–Sawyer limits.

The advantage of simulated data with linear and nonlinear constitutive relations coupled to the momentum equations is that one can explore signatures of nonlinearity beyond the measurable data. The most recent approaches in lung biology recognize that linear viscoelasticity of mucus is important, but nonlinearity is assumed to be confined to a small boundary layer where the cilia engage. We are interested in whether nonlinearity is localized at the driven interface, or if it penetrates successively into the layer with increased forcing, or whether the shear waves generated at the driven boundary set up interference patterns that could divide the layer into sub-layers of linear and nonlinear response. It is possible,

* Corresponding author. Tel.: +1 3025078328.
E-mail address: vasquezpaula02@gmail.com (P.A. Vasquez).

0377-0257/$ - see front matter © 2013 Elsevier B.V. All rights reserved.
http://dx.doi.org/10.1016/j.jnnfm.2012.12.016

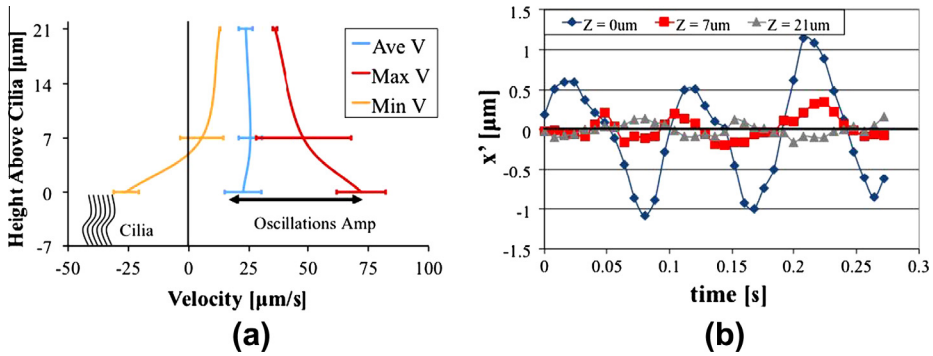

Fig. 1. Analysis of mucociliary transport in HBE cultures. (a) Bead velocity data above the mucociliary interface. (b) Height-dependent bead displacement time series showing amplitude attenuation and evidence of bi-directional shear waves.

although we confide up front that we have not succeeded, that modeling studies may point to new experimental probes for inference of nonlinear properties analogous to recent advances in LAOS [8–10]. We are interested in all aspects of the heterogeneous layer, including shear and normal stresses, strains and strain rates, and in their correlations both temporal and spatial. It is not *a priori* obvious or known which of these features provides the most easily detected signature of nonlinearity, nor whether the critical yield criterion is a stress, strain or strain rate threshold.

These cell culture observations are reminiscent of Stokes' second problem concerning quasi-steady shear waves in an unbounded domain above a plane oscillating at a fixed frequency. Ferry, Adler, and Sawyer [1,2] extended Stokes' second problem to linear viscoelastic materials and devised a shear wave rheometer based on explicit solutions of the equations of linear viscoelasticity in a semi-infinite domain. Solutions of the resulting system of equations, for each frequency of plate oscillation, give a one-to-one relation between the attenuation and oscillation length scales of the shear wave and the dynamic moduli of the material; see Eq. (6) below. The method relies on polymeric liquids that are both semi-transparent and strain-birefringent.

In contrast to this "shear wave rheometer", modern commercial rheometers operate at sufficiently small gap heights that heterogeneous features cannot form, i.e., gaps are smaller than the attenuation and oscillation length scales of the material [2,11]. In this so-called gap-loading limit, the hydrodynamics is controlled as a linear shear wave, and the viscoelastic response (linear and nonlinear) is dictated by the frequency and amplitude of the imposed plate motion. Most importantly, there is no feedback between viscoelastic stresses and hydrodynamics, the spatial dependence is completely known, and time-dependent ordinary differential equations (ODEs) govern stress response for imposed strain. This decoupling of the viscoelastic response from the momentum balance equations has afforded significant progress in the study of large-amplitude oscillatory shear (LAOS) restricted to the gap-loading limit, including recently introduced metrics for nonlinearity [8–10], and evaluation of constitutive equations and their parameters [12,13].

However, conditions in cell cultures or in millimeter-scale parallel plate shear cells preclude the use of these studies to interpret the observational data: the primary flow is an arbitrary shear and the stresses are heterogeneous. In the gap-loading limit, the strain rate, strain, and driving frequency are controlled at every gap height and completely correlated, so that the amplitude of the shear stress is constant across the gap. However, in the intermediate-gap regime *all controls on stress and strain are lost except at the plates*; heterogeneity couples stress and strain fields, so that nonlinearity propagates from the uncontrolled stress at the plates into the gap. Because shear and stress waves reflect off each boundary, there is no *a priori* guarantee how these features will constructively or destructively interfere, and therefore the layer heights of nonlinear and linear response are unpredictable. The quasi-stationary response, after transients have passed, is easily and explicitly derived in the linear viscoelastic regime. However, the nonlinear response is nontrivial, and specific to the material in question or the presumed nonlinear constitutive law. In lung biology, it is easy to imagine how focusing of nonlinear response might promote mucus transport: a shear-thinned layer near the cilia interface could provide a lubrication layer, allowing the "un-thinned" fluid above to translate as a plug. An internal thinned layer might allow a fraction of the mucus layer to translate relative to the rest of the layer. The existence of such scenarios, and the conditions under which they arise, motivate this study; again, we use a different geometry to probe these questions in order to reduce space dimensionality and computational complexity.

We consider gap heights on the order of millimeters, which support heterogeneous bi-directional shear waves. An example of experiments in a similar geometry is the work of Winet et al. [14], who studied mucociliary flow over frog palates with mucus layers up to 0.9 mm. Our focus here is to characterize the diverse behavior from weakly to strongly nonlinear viscoelastic fluids and constitutive laws in this geometry. The phenomena we explore are natural consequences of heterogeneous standing waves of deformation and stress in this intermediate gap height regime. The study is carried out using one of the canonical nonlinear constitutive laws of continuum viscoelasticity, the Giesekus model, with tunable parameters to explore effects of nonlinearity.

The main challenge in choosing an appropriate constitutive equation for biological fluids in general, and mucus in particular, is the multiple modes necessary to capture even the linear viscoelastic data. Data obtained in the Hill lab shows that to accurately match mucus dynamic moduli in small amplitude oscillatory shear, over a physiological frequency range, it is necessary to superimpose approximately 10 discrete linear viscoelastic modes. Rather than perform simulations of 10 coupled Giesekus tensorial constitutive equations together with the hydrodynamic equations, we instead model the linear and nonlinear behavior of a single nonlinear viscoelastic mode. For this, we consider model parameters within the range of those measured in mucus across physiologically relevant concentrations: 1.5–5 wt.%; i.e., a modulus of 10 Pa and a relaxation time of 1 s.

In the rest of the paper, we first describe the theoretical modeling and numerical tools used in our protocol. We then summarize nonlinearity metrics that have been developed for gap-loading experiments on viscoelastic materials, and explain their limitations with regard to the proposed heterogeneous oscillatory shear experiments. We perform numerical studies and apply nonlinearity metrics to illustrate the phenomenon of interest for this paper:

partial penetration of nonlinearity, distributed non-uniformly within the gap, in finite depth viscoelastic layers in oscillatory shear.

2. Model formulation

The system consists of a layer of incompressible viscoelastic fluid of height, H, trapped between two plates. The dimensions of the plates are assumed much greater than the plate gap so that those boundary conditions are negligible over the course of the experiment. The fluid is set into motion by an oscillating lower plate with imposed translational velocity along a fixed axis, $U = U(t)$. It is assumed that the upper plate remains flat and parallel to the lower plate. For completeness, here we briefly discuss the formulation developed in previous work [3–5]. In this work $\mathbf{v}'(\mathbf{x},t)$, $p'(\mathbf{x},t)$ and $\boldsymbol{\tau}_p'(\mathbf{x},t)$ denote, respectively, the velocity, pressure and extra stress fields, and the primes denote dimensional variables.

2.1. Governing equations

- *Conservation of mass and momentum*
  By symmetry, the one dimensional wave propagation problem leads to the following reductions: $p = p(y,t)$, $v_x = v_x(y,t)$, $v_y = 0$, $v_z = 0$, $\boldsymbol{\tau}_p = \boldsymbol{\tau}_p(y,t)$ with $\tau_{p\,xz} = \tau_{p\,yz} = 0$. With these, the equation for the conservation of mass is automatically satisfied and the conservation of momentum reduces to a scalar equation,

$$\rho \frac{\partial v_x'}{\partial t'} = \frac{\partial \tau_{pxy}'}{\partial y'} + \eta_s \frac{\partial^2 v_x'}{\partial y'^2},$$

  where ρ is the fluid density and η_s is the solvent viscosity. To close this system, a constitutive equation for the extra stress tensor, $\boldsymbol{\tau}_p'$, is necessary. We are interested in differential constitutive models where the extra stress is calculated through some average of the history-dependent conformation of interacting polymer chains, such as the Giesekus model [15].
- *Giesekus model*
  The Giesekus model is based on the concept of anisotropic drag between the solvent and polymer molecules. The latter is represented by Hookean dumbbells immersed in a Newtonian solvent [15,16]. The constitutive equation for the extra stress tensor, following the sign convention from Larson [17], is

$$\frac{\partial \boldsymbol{\tau}_p'}{\partial t'} + (\mathbf{v}'\cdot\nabla')\boldsymbol{\tau}_p' - (\nabla'\mathbf{v}')^T\cdot\boldsymbol{\tau}_p' - \boldsymbol{\tau}_p'\cdot(\nabla'\mathbf{v}') + \frac{\boldsymbol{\tau}_p'}{\lambda} + \frac{\alpha_g}{\eta_p}\boldsymbol{\tau}_p'\cdot\boldsymbol{\tau}_p' = \frac{\eta_p}{\lambda}[(\nabla'\mathbf{v}')^T + (\nabla'\mathbf{v}')],$$

  where α_g is a so-called mobility parameter; λ is the fluid relaxation time; and $\eta_p = \eta_0 - \eta_s$ is the polymer viscosity, with η_0 the material's zero shear viscosity. In this manner, the Upper Convected Maxwell (UCM) model corresponds to the limit $\alpha_g = 0$. Note, here we use the subscript g in the nonlinear parameter of the Giesekus model (α_g), to differentiate it from the reciprocal of the attenuation length of a viscoelastic shear wave defined by Eq. (6) below.

2.2. Non-dimensional equations

The following characteristic scales are used in the non-dimensionalization of the resulting system of equations,

$$t = \frac{t'}{\lambda}, \quad \mathbf{x} = \frac{\mathbf{x}'}{H}, \quad \mathbf{v} = \frac{\mathbf{v}'}{H/\lambda}, \quad \boldsymbol{\tau}_p = \frac{\boldsymbol{\tau}_p'}{G_0}, \quad p = \frac{p'}{G_0}.$$

With this scaling the conservation of momentum becomes,

$$\frac{\partial v_x}{\partial t} = \frac{1}{El}\left[\frac{\partial \tau_{pxy}}{\partial y} + \beta_s \frac{\partial^2 v_x}{\partial y^2}\right], \tag{1}$$

where the Elasticity number, $El = \rho H^2/(\eta_0\lambda) = Re/We$, is the ratio of elastic to inertial forces. With our scaling, the Weissenberg number corresponds to the non-dimensional amplitude of the bottom plate velocity, $We = \lambda U_0/H$, and the Reynolds number is $Re = \rho U_0 H/\eta_0$. In addition, we assume $\beta_s = \eta_s/\eta_0 \ll 1$, so that the solvent viscosity is negligible relative to the polymeric viscosity.

In the same manner, the non-dimensional Giesekus constitutive equation becomes

$$\frac{\partial \boldsymbol{\tau}_p}{\partial t} - (\nabla\mathbf{v})^T\cdot\boldsymbol{\tau}_p - \boldsymbol{\tau}_p\cdot(\nabla\mathbf{v}) + \boldsymbol{\tau}_p + \frac{\alpha_g}{1-\beta_s}\boldsymbol{\tau}_p\cdot\boldsymbol{\tau}_p = (1-\beta_s)[(\nabla\mathbf{v})^T + (\nabla\mathbf{v})]. \tag{2}$$

Note that with our scaling the Deborah number is the non-dimensional driving frequency, $De = \lambda\omega$, so that the non-dimensional velocity at the moving boundary is given by,

$$v_x(0,t) = We\cos(De\,t). \tag{3}$$

From Eq. (3) we see that the limit $De \to 0$ corresponds to steady viscometric flow, while $We \to 0$ is the linear viscoelastic limit, often called small amplitude oscillatory shear (SAOS). Note also that the bulk strain is $\gamma_0 = A/H = We/De$, where the maximum amplitude of the plate is $A = U_0/\omega$. In this work, we will analyze departures from linear behavior in terms of these dimensionless groups, which in the gap loading limit are classically compiled in phase diagrams in the (We,De) parameter space, known as Pipkin diagrams [18]. The heterogeneous extension of the Pipkin diagram is presented in Section 5.3.

To solve the PDE system Eqs. (1) and (2) we implement a wave propagation algorithm as in [3]. There it was shown that the boundary conditions can only be imposed on either the stress or the velocity at each boundary, while the remaining variables are dictated by characteristic data. In this work we impose boundary conditions on fluid velocity, unless otherwise noted. At the top plate the velocity is set to zero, $v_x(t,H) = 0$, and a simple harmonic motion is imposed on the bottom plate. In the latter, instead of an instantaneous jump in the velocity, we use a 'ramp' of the form,

$$v_x(t,0) = We\tanh(b\,t)\cos(De\,t). \tag{4}$$

The choice of the parameter b only affects the transient part of the time series and not the quasi-steady state, as shown in Fig. 2. We use $b = 10\ \mathrm{s}^{-1}$ for all our simulations.

3. Gap height bounds for the gap-loading and surface-loading regimes

Consider a viscoelastic fluid placed between two parallel planar boundaries, one fixed and the other undergoing sinusoidal displacements. Under these conditions shear waves are launched from the moving boundary, and if the effects of side walls and non-parallelism of the plates are negligible, they propagate as one-dimensional disturbances toward the opposing boundary. This propagation depends both on the properties of the fluid and on the size of the gap. Based on the interplay between these two conditions, we can differentiate three cases. First, in the *gap-loading limit* the gap between the plates is sufficiently narrow, so that waves are unable to form, inertial effects can be neglected, and the sample moves in phase with the driving surface. In this case, a uniform shear rate profile evolves within the gap. These conditions are exploited in essentially all commercial shear rheometers. Second, if the wave attenuation scale is larger than the gap height, reflection occurs and bidirectional waves lead to distinct standing shear wave patterns. In this intermediate gap height regime, we will show that a wide range of behaviors arise depending on the wavelength of the oscillation relative to the gap height and of

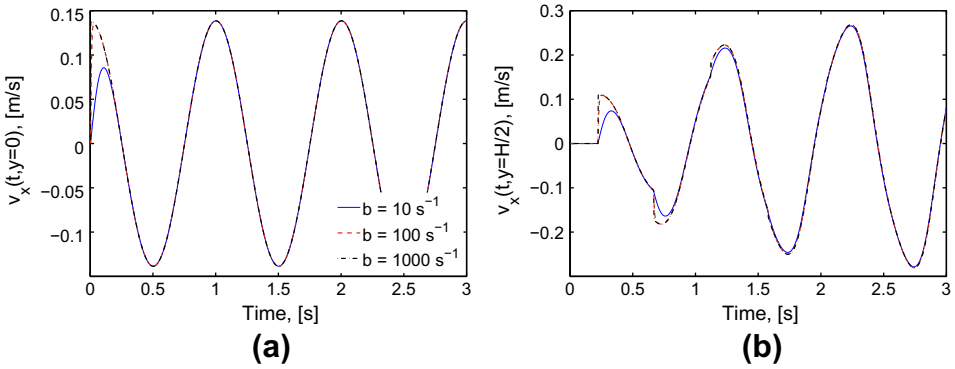

Fig. 2. Numerical protocol for onset of plate motion and initial transient. (a) Imposed velocity $v_x(t,0) = We\tanh(bt)\cos(De\,t)$ at the driving plate. (b) Early transient velocity in the middle of the gap corresponding to the profiles shown in figure (a). Results using the Giesekus model.

course the amplitude of the imposed boundary motion. The extension to intermediate gap heights for linear and nonlinear driving amplitudes was studied previously in [3–5]. Casanellas and Ortín [19] also recently studied this limit investigating the flow of an upper convected Maxwell fluid between two plates oscillating synchronously. Third, if the shear waves have sufficient room to develop and yet decay nearly to zero before reaching the top plate, the experiment conforms to Stokes' second problem, as exploited by Ferry et al. [1,2]. This case is known as the *surface-loading limit*.

Here it is important to point out that the heterogenous behavior investigated in this work is not to be confused with the highly studied phenomenon of shear banding that arises, at critical shear rates, from flow instabilities in the gap-loading limit. For this case inhomogenous strain rate profiles are observed within the gap and inhomogeneities gradually disappear at high frequencies. This occurs because the system does not have enough time to relax and shear bands cannot form completely within a cycle [20,21]. On the contrary, the nonlinear behavior we study here has its origins in the constructive and destructive interference of counter-propagating shear waves and associated stress profiles. In this case, the strain rate varies continuously throughout the gap for all material parameters and driving conditions. We note that the nonlinear behavior is also attenuated as the frequency increases.

Before we investigate the heterogenous limit, we pause to analyze *a priori* bounds on the gap-loading, intermediate-gap, and surface-loading regimes. This can be done analytically in the case of linear viscoelastic materials. Here we follow Schrag [11] who characterized the gap-loading limit in terms of the velocity gradient. We translate this argument into an upper bound on the gap height, H, in terms of linear dynamic moduli. In this section we use dimensional variables, since we want to keep H explicitly in the equations, but we omit the prime notation.

In the linear viscoelastic limit, for a stationary top plate, and given the following driving condition at the bottom plate,

$$v_x(0,t) = U_0 e^{i\omega t},$$

the velocity profile at any point within the gap is given by,

$$v_x(t,Y) = U_0\frac{\sinh(\delta Y)}{\sinh(\delta H)}e^{i\omega t}, \tag{5a}$$

$$\delta = \alpha + i\beta. \tag{5b}$$

with $Y = H - y$, and we use complex notation for convenience, α and β are, respectively, the *reciprocal attenuation and oscillation length scales* of unidirectional waves. For a detailed derivation of Eq. (5a) see [3]. For the UCM model, and therefore linearized Giesekus model, these reciprocal lengths are given by [2,3],

$$\alpha = \sqrt{\frac{\rho\omega^2}{2}\left(\frac{1}{|G^*|} - \frac{G'}{|G^*|^2}\right)}, \quad \beta = \sqrt{\frac{\rho\omega^2}{2}\left(\frac{1}{|G^*|} + \frac{G'}{|G^*|^2}\right)}, \tag{6}$$

where the complex modulus is $G^* = G' + iG''$. Here the storage modulus, G', captures the elastic effects, while the loss modulus, G'', captures the viscous effects. It can be shown that for viscous fluids $\alpha/\beta = 1$, whereas for elastic solids $\alpha/\beta = 0$. Viscoelastic fluids span these two limiting cases. We again caution the reader to not confuse the wave parameter α with the Giesekus nonlinearity parameter α_g.

From Eq. (5a) the velocity gradient is,

$$\frac{\partial v_x}{\partial Y} = v_{x,Y} = U_0\delta\frac{\cosh(\delta Y)}{\sinh(\delta H)}e^{i\omega t}. \tag{7}$$

In the gap-loading limit, stress and strain should be approximately uniform in the gap, the instantaneous velocity profiles across the gap are linear, and the shear rate is independent of position [2,11]. That is, in this limit the velocity gradient is given, to first order, by

$$v^{GL}_{x,Y} = \frac{U_0}{H}e^{i\omega t} + O(H).$$

This behavior is insured if $|\delta H| \ll 1$, which renders $\cosh(\delta Y) \sim 1$. Likewise, Eq. (7) can be manipulated to show

$$|v_{x,Y}| = U_0\sqrt{\alpha^2+\beta^2}\sqrt{\frac{\cosh^2(\alpha Y) + \cos^2(\beta Y) - 1}{\cosh^2(\alpha H) - \cos^2(\beta H)}}.$$

As a consequence of $\left|v^{GL}_{x,Y}\right|$ being constant in space, and following Schrag [11], *we look for conditions where* $|v_{x,Y}|/\left|v^{GL}_{x,Y}\right|$ *exhibits spatial variation as the signature for departures from the gap-loading limit*. The formulas above yield a separable form of this ratio:

$$\frac{|v_{x,Y}|}{\left|v^{GL}_{x,Y}\right|} = \left[\sqrt{\frac{(\alpha H)^2 + (\beta H)^2}{\cosh^2(\alpha H) - \cos^2(\beta H)}}\right] \times \left[\sqrt{\cosh^2(\alpha Y) + \cos^2(\beta Y) - 1}\right]. \tag{8}$$

The second factor in Eq. (8) captures all spatial dependences, and so we normalize the velocity gradient one step further to isolate this dependence. We define a normalized velocity gradient, $\tilde{\nabla} v$, by,

$$\tilde{\nabla} v = N\frac{|v_{x,Y}|}{|v^{GL}_{x,Y}|} = \sqrt{\cosh^2\left(\frac{\alpha}{\beta}\beta Y\right) + \cos^2(\beta Y) - 1}, \tag{9}$$

where N is the reciprocal of the first factor in Eq. (8). Since $\tilde{\nabla} v$ depends only on βY and α/β (which lies between 0 and 1), the master plot shown in Fig. 3 captures the spatial variations of $\tilde{\nabla} v$ for any viscoelastic material whose properties are given by α and β, or

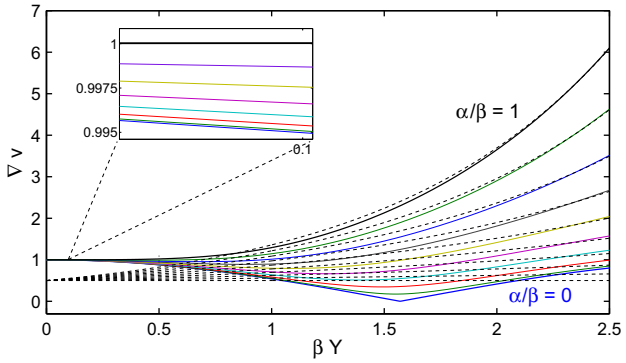

Fig. 3. Solid lines represent the normalized velocity gradient $\bar{\nabla} v$ versus βY for values of $0 \leqslant \alpha/\beta \leqslant 1$ from Eq. (9). Inset shows that the gap-loading approximation is valid for $\beta Y < 0.1$. Dashed lines are for $\bar{\nabla} v$ in the surface-loading limit, Eq. (10).

equivalently by its dynamic moduli, see Eq. (6). Note that whenever $\beta Y \lesssim 0.1$, differences between the velocity gradient for all α, β, and Y, is less than 5% (see inset in Fig. 3). This is the signature of the gap-loading regime, and gives the following bound for the gap height in the gap loading limit: $H \leqslant 1/(10\beta)$.

Next, we follow a similar argument to determine limits for the surface-loading regime. In this limit the velocity is given by [2],

$$v_x(t,y) = U_0 e^{i(\omega t - \delta y)},$$

and the resulting normalized velocity gradient is,

$$\bar{\nabla} v = N\frac{|v_{x,Y}|}{|v_{x,Y}^{GL}|} = \frac{1}{2}e^{\alpha Y} = \frac{1}{2}e^{(\alpha/\beta)(\beta Y)}. \tag{10}$$

Here Y, N and $|v_{x,Y}^{GL}|$ are defined as before. Plots of this limit are shown in Fig. 3 by dashed lines. For the surface loading limit the condition on the height is $H \gg 1/\alpha$ and is highly dependent on the material properties.

Finally, we can also define bounds for heights in the intermediate gap regime. In general for any viscoelastic fluid the requirement is that the sample thickness accommodates the wavelength of the propagating shear wave, i.e., H is of order $1/\beta$ or larger. To express this limit as a function of material parameters, we use Eq. (6). Since $\beta \geqslant \alpha$, the bounds for any viscoelastic material in the intermediate gap height are approximated by $1/\beta \leqslant H \leqslant 1/\alpha$.

Note that the formulation of Eq. (6) includes the assumption $\eta_s = 0$. However, it can be shown that the functional form of α and β remains the same after introducing a solvent viscosity, e.g., using the Oldroyd B model instead of UCM. In this case the complex modulus is $G^*(\omega) = G'(\omega) + \eta_s\omega + iG''(\omega)$. Asymptotic analysis for small solvent viscosity shows that while the oscillation wave length ($2\pi/\beta$) always increases with the addition of a solvent, the attenuation length ($1/\alpha$) may decrease or increase depending on the relation between the elastic and viscous components of the complex modulus. To first order, addition of solvent viscosity increases the attenuation length, or equivalently the damping of the shear wave occurs on longer length scales, if

$$G'' > \sqrt{3}G'.$$

4. A review of LAOS metrics in rheometric and non-rheometric flows

The simplest model for a nonlinear viscoelastic material is the Upper Convected Maxwell (UCM) model, whose constitutive equation in non-dimensional form is

$$\frac{\partial \boldsymbol{\tau}_p}{\partial t} - (\nabla \mathbf{v})^T \cdot \boldsymbol{\tau}_p - \boldsymbol{\tau}_p \cdot (\nabla \mathbf{v}) + \boldsymbol{\tau}_p = (1-\beta_s)[(\nabla \mathbf{v})^T + (\nabla \mathbf{v})]. \tag{11}$$

In the limit of small deformations the Giesekus model reduces to the UCM model and fittings to experimental data in this regime, for example to small amplitude oscillatory shear (SAOS), give values for the relaxation time, λ, and the modulus, G_0. The storage and loss moduli for the UCM model are [16],

$$G'(\omega) = G_0\frac{(\lambda 2\pi\omega)^2}{1+(\lambda 2\pi\omega)^2}, \quad G''(\omega) = G_0\frac{\lambda 2\pi\omega}{1+(\lambda 2\pi\omega)^2}, \tag{12}$$

here the frequency, ω, has units of Hz. Using Eqs. (6) and (12), we can now estimate bounds on the gap height, H, that insure the gap-loading limit for different materials, by $H^* < 1/(10\beta)$. Table 1 shows the parameter values for three representative viscoelastic fluids and their calculated H^*. Recall that we defined the intermediate-gap regime for heights $1/\beta \leqslant H \leqslant 1/\alpha$. From Table 1 we see that while the lower bounds for the viscoelastic and strongly elastic fluids are comparable, their upper bounds differ by one order of magnitude. This is a consequence of the viscoelastic wave being more damped than a pure elastic wave.

4.1. Resonance heights of the shear gap

For a viscoelastic fluid confined between two parallel plates and given a shear wave speed c, a shear wave launched from an oscillating bottom plate at period $2\pi/\omega$ will travel a distance $L_r = 2\pi c/\omega$ in one period of the plate motion. Lindley et al. [5] investigated the spatial distribution of shear and normal stresses for three model materials and several H/L_r ratios. They found that the viscoelastic response shows non-monotonicity of stresses within the gap with respect to the gap position, y, for fixed material parameters, gap height and driving conditions, and with respect to changes in gap height and material properties, for all other parameters fixed, respectively. And they showed that there are large domains in the full parameter space where the maximum shear stress occurs within the interior of the gap, as opposed to the driving boundary. Following [5], we define a *resonance height* $H_r = L_r/2 = \pi c/\omega$ specified by the shear wave speed,

$$c = \sqrt{\frac{G_0 + \tau'_{yy}}{\rho}}. \tag{13}$$

Here, as in Table 1, we take $G_0 = 10$ Pa and we assume the density to be comparable to that of water, $\rho \sim 1000$ kg/m^3. Then, for the UCM model Eq. (13) becomes,

$$c_L = \sqrt{\frac{G_o}{\rho}} = 0.1 \text{ m/s}. \tag{14}$$

In this case $H_r = 0.1/2 = 5$ cm for $\omega = 1$ Hz. For nonlinear viscoelastic responses, $\tau_{yy} \neq 0$ so that the "resonant height" is not well-defined, and if so only in an averaged sense, since the wave speed of the nonlinear solution for v_x, τ_{xy}, τ_{xx} and τ_{yy}, varies in both space and time. In Section 5.1.2 we discuss the procedure we follow to specify a resonance height.

4.2. Large Amplitude Oscillatory Shear (LAOS)

4.2.1. Review of LAOS analysis in the gap-loading (homogeneous) limit

In the gap-loading regime, linear viscoelasticity, often called small amplitude oscillatory shear (SAOS), implies that the material properties are determined by measurements of the shear stress amplitude, τ_0, and the phase angle, δ, between the stress and the applied strain, $\gamma = \gamma_0\sin(\omega t)$: $\tau(t) = \tau_0\sin(\omega t + \delta)$. The dynamic moduli are given by $G' = G'(\omega) = (\tau_0/\gamma_0)\cos(\delta)$ and $G'' = G''(\omega) = (\tau_0/\gamma_0)\sin(\delta)$ [2]. If the strain amplitude, γ_0, is increased

Table 1
Fluid parameters. Here $G_0 = \eta_0/\lambda = 10$ Pa for all three fluids, and $\omega = 2\pi$ rad/s. In this work we consider gap heights on the order of cm, which correspond to the intermediate gap regime for all three fluids.

Fluid	η_0 (Pa s)	λ (s)	α/β	G'/G''	$1/\alpha$ (mm)	$1/\beta$ (mm)	H^* (mm)
Strongly elastic	100	10	0.0080	62.832	2000.1	15.915	1.592
Viscoelastic	10	1	0.0791	6.2832	200.63	15.866	1.586
Nearly viscous	0.1	0.01	0.9391	0.0628	5.8218	5.4675	0.547

systematically to enter the nonlinear viscoelastic regime, the resulting tests are known as large amplitude oscillatory shear (LAOS), and the stress response, although constant across the gap, is no longer restricted to the fundamental harmonic of the strain. Analyzing data for rheological significance obtained from LAOS experiments is not straightforward, and several protocols have been proposed. For an excellent recent review, we refer to [22]. The most common methods of interpreting LAOS data are Fourier transform (FT) rheology [23–25], Lissajous–Bowditch curves [23], stress decomposition (SD) into elastic and viscous stress contributions [8,26], description of these contributions by orthogonal Chebyshev polynomials [9], and the analysis of the stress temporal waveforms as a sequence of physical processes [10].

Lissajous–Bowditch curves offer a qualitative analysis of the stress waveforms. Elastic Lissajous–Bowditch curves show the oscillatory stress as a parametric function of the input strain, whereas in viscous Lissajous–Bowditch curves one plots the stress against the rate of strain. In this way, for an elastic solid, the elastic Lissajous–Bowditch curves are represented by straight lines and viscous Lissajous–Bowditch curves by circles, while the opposite is true for a viscous fluid. In the small amplitude regime for a generic viscoelastic fluid, both Lissajous–Bowditch curves are ellipses. Departures from an ellipse signal that the nonlinear LAOS regime has been reached.

FT rheology decomposes stress time-domain series into a frequency dependent spectrum and deviations from linear behavior are studied by comparing relative intensities of higher harmonics with respect to the fundamental harmonic, I_n/I_1 [25],

$$\tau_{xy}(t;\omega,\gamma_0) \propto I_1(\gamma_0)\cos(\omega t) + I_3(\gamma_0)\cos(3\omega t) + I_5(\gamma_0) \times \cos(5\omega t) + \ldots \quad (15)$$

The coefficients are found in the usual manner by Fourier analysis, either from experimental or numerical data. In particular, the magnitude of the third harmonic, I_3, besides being a metric to indicate departures from linear behavior, can be also viewed as a nonlinear material property. To this end, Hyun and Wilhelm [27] proposed the following nonlinear coefficient: $Q = I_3/\gamma_0^2$. At small strain amplitudes, but still within the LAOS regime, this coefficient is a constant, Q_0. This limit of small strain amplitude is known as the medium amplitude oscillatory shear (MAOS) [27].

Other approaches to the analysis of LAOS data are based on the fact that the shear stress can be written as a time-domain Fourier series of odd-harmonics [28]

$$\tau_{xy}(t;\omega,\gamma_0) = \gamma_0 \sum_{n:\text{odd}} \left[G_n' \sin(n\omega t) + G_n'' \cos(n\omega t)\right], \quad (16)$$

Cho et al. [8] proposed a stress decomposition (SD) into elastic and viscous contributions based on geometric considerations. They show that these contributions are one-to-one functions of the strain and the strain rate respectively, so that they become one-dimensional lines in the elastic and viscous Lissajous–Bowditch curves. This overcomes the problem of characterizing two-dimensional ellipses in the Lissajous–Bowditch curves. The authors suggested a polynomial regression fit to these single-valued curves as a mean to characterize nonlinearities.

Yu et al. [26] generalized the SD method so that any signal is decomposed into Fourier series without limitations on odd or even harmonics as in the SD method. That is, they decompose the signal into four parts, one for the odd harmonics of the sine function, one for the odd harmonics of the cosine function, one for the even harmonics of the sine function, and one for the even harmonics of the cosine function. The coefficients are then determined by polynomial fitting to orthogonal Chebyshev polynomials of the first and second kind. This approach allows for the analysis of transient data and normal stresses, as well as data from experiments with non-sinusoidal input, e.g., superimposed oscillatory shear flow.

Ewoldt et al. [9] extended the stress decomposition (SD) method by expanding the elastic and viscous components in terms of Chebyshev polynomials of the first kind. The authors proposed several metrics to characterize nonlinear viscoelasticity. These metrics have a direct geometrical representation in the Lissajous–Bowditch curves (see Fig. 3 in [9]), and have the advantage of not being based on individual harmonic contributions. Läuger and Stettin [29] extended this framework to minimum-and large-stress compliances and fluidities in the case of stress-controlled tests.

Finally, Rogers et al. [10] argue that a more physical description of the nonlinear behavior in LAOS can be attained if the responses are represented by a sequence of purely elastic to purely viscous physical processes. They defined a pair of parameter metrics for nonlinearity: $[A'_{\min}, \theta_c]$. The first parameter is the *minimum unsigned area* enclosed by the projection of the elastic Lissajous–Bowditch curve under rotations about the $z-$axis. The second parameter, θ_c is the angle at which this minimum is attained. In this way, $A'_{\min,} > 0$ signals deviations from linear viscoelastic behavior and the total stress response can be then characterized as "predominantly elastic": $\theta_c < \pi/4$ or "predominantly viscous": $\theta_c > \pi/4$.

All of these analyses are restricted to the gap-loading limit; they are model independent; and inferences about linear and nonlinear response are based solely on measured data at the driven plate under the assumption that the stress and rate of strain are uniform throughout the gap. In the next sections we will show that, in the heterogeneous limit, all these metrics are also functions of space, and measurements only at the plate are oblivious to, and are insufficient to infer, a rich set of linear and nonlinear behavior that evolves within the gap.

4.2.2. LAOS in the intermediate gap height regime

Our interest here is in gap heights that support shear wave features and thereby nontrivial stress gradients, but that are small enough to avoid damping of the shear waves before reaching the opposing boundary. Loosely, the gap height, H, lies between $1/\beta$ (oscillation length) and $1/\alpha$ (attenuation length), as discussed in Section 3. Thus the gap response, after transients, consists of constructive and destructive interferences of bi-directional waves of strain, strain rate, shear stress, and normal stresses. *This heterogeneous behavior could be experimentally observed by particle tracking, simply by detection of higher harmonic generation of time series of particle position in the gap interior. However, the inferences that can be drawn from the data are not well understood*. Instead, here we use numerical models to explore and predict this behavior and to learn the extent to which the behavior can be predicted from known properties of the fluid. This latter issue is prerequisite to any future progress on the use of models together with data for the inverse problem, i.e., to infer nonlinear rheological properties.

As a first step in this process, we explore the behavior, within the gap, of some of the metrics used in the gap-loading regime. The purpose of Section 5.2 is to represent the internal gap dynamics in the standard metrics of LAOS, which will reveal how these metrics breakdown outside the gap-loading limit.

Recall that the analysis of both SAOS and LAOS data is restricted to standard stress-or strain-controlled rheometers in the gap loading limit. In this limit, a single-harmonic sinusoidal stress (or strain) is imposed throughout the gap. The typical LAOS analysis therefore is a mapping from a controlled linear harmonic mode (e.g., the strain) to the shear stress. Outside the gap-loading limit, and once nonlinearities arise, coupling between velocity and stresses results in the violation of these assumptions, potentially everywhere away from the driven plate. If one variable has higher harmonics at a given gap height, it is expected that all other variables at that height will reflect higher harmonics. Hence, inference of material responses inside the gap are given by the correlations between the time series of strain and stress. Numerically, these correlations depend on the nature of the constitutive relations that govern the fluid. Furthermore, the fact that in the heterogeneous limit the stress and strain can be written as,

$$\tau_{xy}(t,y;\omega,\gamma_0) = \gamma_0 \sum_{\text{n:odd}} \left[G_n'(y;\omega,\gamma_0)\sin(n\omega t) + G_n''(y;\omega,\gamma_0)\cos(n\omega t)\right], \tag{17}$$

$$\gamma(t,y;\omega,\gamma_0) = \gamma_0 \sum_{\text{n:odd}} \left[\gamma_n'(y;\omega,\gamma_0)\sin(n\omega t) + \gamma_n''(y;\omega,\gamma_0)\cos(n\omega t)\right], \tag{18}$$

limits the use of some of the metrics described in the previous section which were formulated assuming that the only nonzero component of the strain series is γ_1'.

We explore these correlations between stress and strain in the next section by direct numerical simulations of the coupled system of hyperbolic PDEs for finite depth viscoelastic layers in oscillatory strain driving conditions.

5. Nonlinear phenomena for intermediate gap heights

In this section we present solutions of the PDE system Eqs. (1) and (2) taking representative material parameters from Table 1, i.e., $\eta_0 = 10$ Pa s and $\lambda = 1$ s. We consider two viscoelastic constitutive laws. The first one is the Upper Convected Maxwell (UCM) model, which has the property that the velocity and shear stress, after transients pass, obey the same *damped linear wave equations* [3], but with different boundary conditions. One consequence of this linear behavior is that additional nonlinear terms in the differential constitutive equation are required to generate nonlinear LAOS responses. For this we use the Giesekus model, and we fixed its mobility parameter, $\alpha_g = 0.35$, in all the simulations.

Analyses of the solutions to the PDE system are based on the observed behavior of the velocity and stress components in both time and space. As an illustration of typical solutions, in Fig. 4 we show the time evolution and spatial distribution of the velocity calculated with the UCM model. Fig. 4a plots typical time evolutions of the UCM velocity at different positions in the gap. That figure shows that the quasi-steady state, after transients have passed, is achieved at different times in the gap. We allow transients to pass at *all* points in the gap, and focus on the quasi-steady velocity (equivalently strain) and stress components. These time series are then investigated through their Fourier decomposition.

We calculate the Fourier coefficients of the time series of any feature $\chi(t,y)$ at each height in the gap as,

$$a_n(y) = \frac{1}{\pi}\int_0^{2\pi\omega} \chi(t,y)\sin(2\pi n\omega t)dt, \quad b_n(y) = \frac{1}{\pi}\int_0^{2\pi\omega} \chi(t,y)\cos(2\pi n\omega t)dt, \tag{19}$$

where $0 \leqslant y \leqslant H$ and $\chi(t,y)$ can be the velocity, strain, strain rate, shear stress or first normal stress difference. Although early transient behavior has non-vanishing even harmonics [30], we only consider the quasi-steady response that only possesses odd harmonics.

Finally, we also focus on spatial structure, including snapshot profiles but also the spatial distribution of the Fourier spectrum Eq. (19) for each flow-stress feature. Fig. 4b dashed lines show snapshots in time of the velocity profile throughout the gap. From these, we construct gap 'envelopes' from the maximum values of the velocity at each height. These envelopes (solid lines) are used to illustrate the effects of different driving conditions and to compare important features across all the variables studied.

In the following sections we solve the UCM and Giesekus models for several conditions to investigate material responses in the intermediate-gap regime through harmonic analysis, Lissajous–Bowditch curves, and Pipkin diagrams discussed below in Section 5.3.

5.1. Harmonic analysis in the intermediate-gap regime

A linear LAOS behavior is characterized by time series of strain and stress whose only harmonic component corresponds to the fundamental frequency. Linear LAOS response is guaranteed for the UCM model, while the Giesekus model may exhibit higher harmonics depending on the driving conditions, the material properties, and the gap height. This section investigates Giesekus model

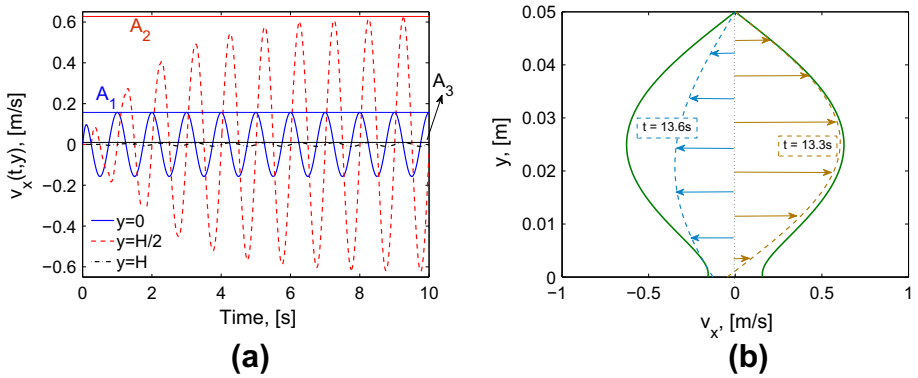

Fig. 4. Velocity features from UCM model: $\lambda = 1$ s, $\eta_0 = 10$ Pa s, $H = 5$ cm, $\gamma_0 = A/H = 0.5$ and $\omega = 2\pi$ rad/s. (a) Velocity at the bottom, middle and top of the gap. Quasi-steady state is achieved at different times in the layer: 1 s at $y = 0$, 9 s at $y = H/2$. (b) Snapshots of the shear wave profile across the gap. Dashed lines show snapshots of the profile, and solid lines represent the envelope of maximum velocities corresponding to the amplitudes in (a), e.g., I_1, I_2, I_3.

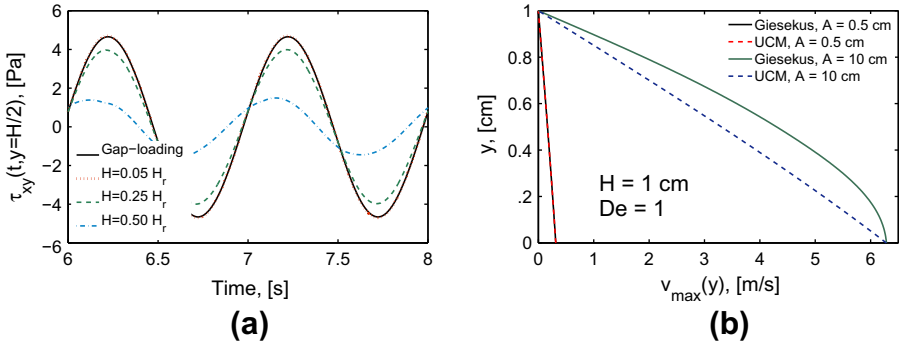

Fig. 5. (a) Giesekus model simulations: Shear stress time series at the mid-gap height ($y = H/2$) versus gap height (H) relative to the resonant height, $H_r = 4.4$ cm. Any $H \leqslant 0.16$ cm corresponds to the gap-loading ODE solution. (b) Onset of nonlinear shear versus amplitude of plate motion. One-sided velocity envelopes from the Giesekus and UCM models for a gap height $H = 1$ cm and two amplitudes of the velocity at the driving plate.

departures from linear LAOS behavior in the intermediate-gap regime *arising solely from changes in gap height*, Deborah and Weissenberg numbers are kept constant, $De = 1$ and $We = 0.5$, while the gap height is varied as multiples of the resonance height, H_r, as defined in Section 4.1.

5.1.1. Linear limits of LAOS in the intermediate-gap height regime

Recall that in this study all simulations with the Giesekus model have $\alpha_g = 0.35$. Furthermore, as discussed in Section 4, the Giesekus model reduces to the UCM model in the limit of small deformations, $\gamma_0 = A/H \to 0$. In the gap-loading regime, the only way of reducing solutions of the Giesekus model to those of the UCM model is by reducing A, since H is bounded, $H \lesssim 0.16$ cm (see Section 3). In the intermediate-gap regime, this limit can be attained by either reducing A and holding H constant, or increasing H while A is kept constant. In this section we show the consequences of these two approaches.

In Fig. 5a the time series of the shear stress at the driving plate are shown for $H \ll H_r$. In addition, the gap-loading solution, for the same driving conditions, is shown by the black line. These plots confirm that the PDE system Eqs. (1) and (2) reduces to the gap-loading results in the limit $H \to 0$. Fig. 5b shows solutions for the UCM and Giesekus models with a gap height $H = 1$ cm (above the gap-loading limit bound) and two values of the amplitude of the driving plate, $A = 0.5$ and 10 cm. Here, nonlinear departures of the Giesekus model are observed as the amplitude is increased, similarly to results in the gap-loading limit. However, in contrast to solutions in the gap-loading limit, the velocity profiles of the Giesekus model are not linear. The main conclusion from both plots in Fig. 5 is that systematic changes in the gap height or the driving amplitude, in the intermediate-gap height regime, holding all other conditions and material properties fixed, result in dramatically different material responses within the gap. Hence, unlike the gap-loading regime, inferences cannot be made based on snapshots or measurements at only one position in the gap, including the driven plate.

Fig. 6a compares the velocity envelopes for the UCM and Giesekus models for two gap-heights. At a height of $H = 0.5H_r$ ($H_r = 5$ cm) the velocities calculated from the two models overlap. Thus at this fixed bulk strain, off-resonant gap heights yield linear response. Note that the resulting velocity is curvilinear, since we are considering heights away from the gap-loading limit. For the same bulk strain but resonant gap height $H = H_r$, however, the two velocity profiles differ in magnitude and shape, indicating a nonlinear response in the Giesekus model. Further characterization of this nonlinear behavior is carried out by analysis of the time series of the shear stress shown in Fig. 6b. Two main differences are observed between the UCM and Giesekus shear stress profiles at different positions within the gap. The first one is related to the amplitude of the time series, which correlates to the amplitude of the velocity profile. Recall that the Giesekus model differs from the UCM model in an extra term which is quadratic in the stress. This term represents "stress-induced acceleration of the relaxation process", resulting in shear-thinning and strain softening [17]. A consequence of this nonlinearity in the constitutive equation is that the amplitudes of both shear stress and velocity are *smaller*

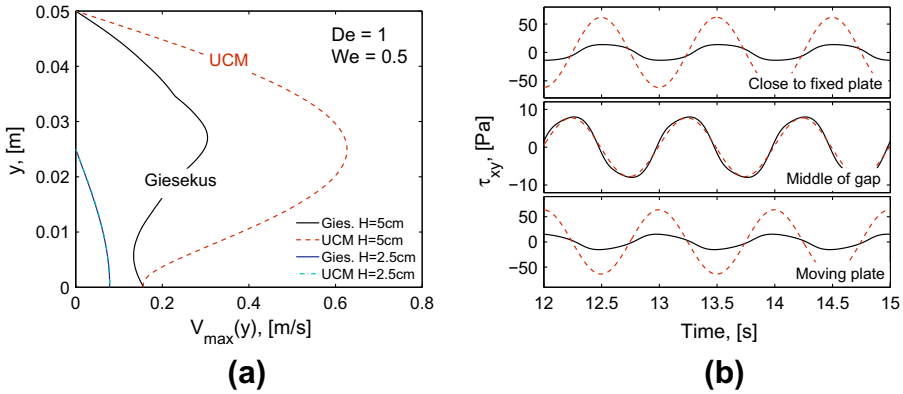

Fig. 6. (a) Velocity envelopes for the UCM and Giesekus models. At small gap heights both curves overlap indicating that the Giesekus model behaves linearly. (b) Time series of shear stress at three places within the gap. Dashed lines correspond to predictions from the UCM model and solid lines from the Giesekus model. Nonlinear behavior in the intermediate-gap regime is characterized by deviations from simple sinusoidal time series for the Giesekus stress. Shear stress profiles corresponding to $H = 2.5$ cm are not shown in the figure, however similar behavior is observed, i.e., Giesekus stress amplitude is smaller, although in this case both profiles have a single sinusoidal form, indicating linear behavior.

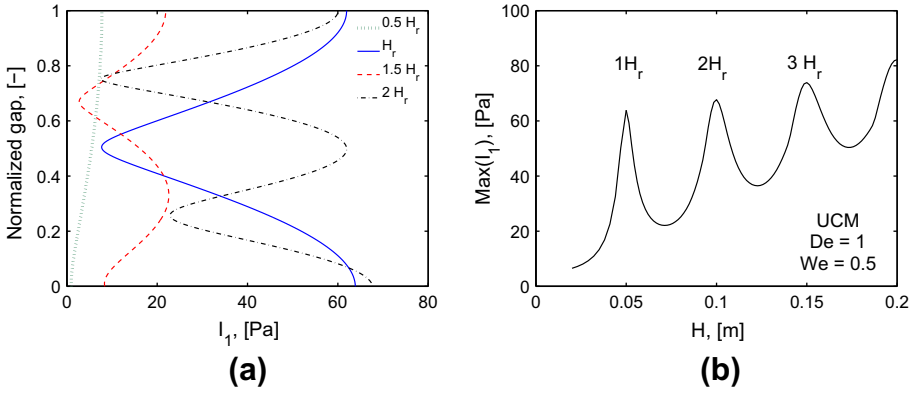

Fig. 7. Resonance in the UCM model. (a) First harmonic distribution of the UCM shear stress calculated for gap heights that are multiples of the resonance height, $H_r = 5$ cm. Higher harmonic components (not shown) are zero for this model. (b) Maximum value of the first harmonic as a function of gap height.

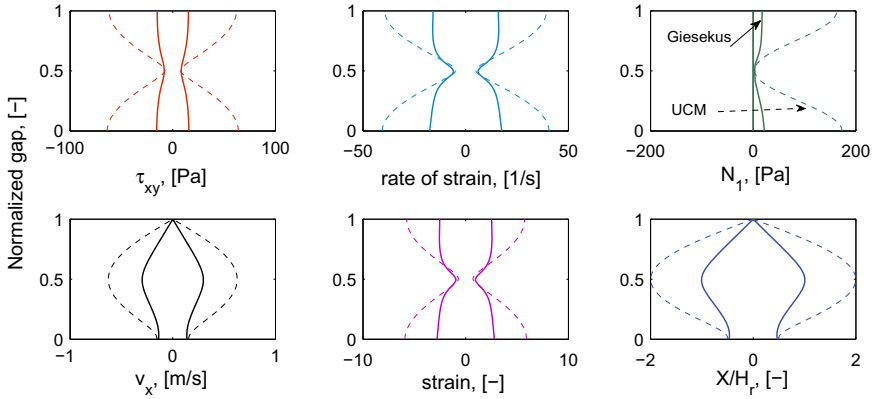

Fig. 8. Contributions from the first harmonic for the UCM (dashed) and Giesekus (solid) models, at their respective resonance heights: $H_r^{UCM} = 5$ cm and $H_r^{G} = 4.4$ cm. For the UCM the first harmonic amplitude corresponds to the full response.

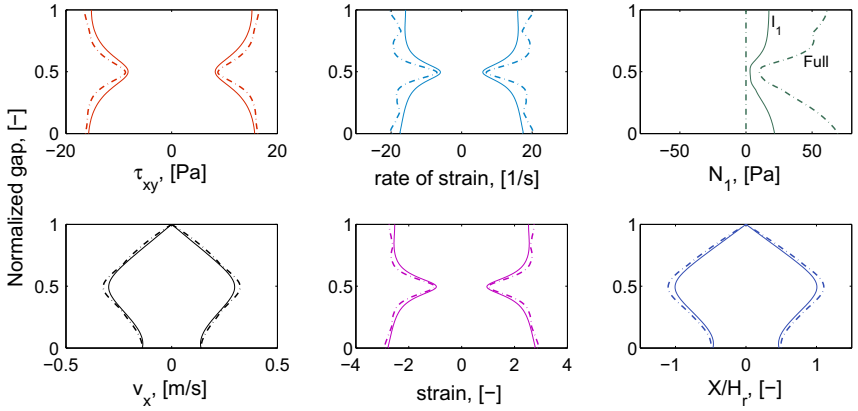

Fig. 9. Full envelopes (dashed lines) for the Giesekus model, and comparison with the amplitude of the Giesekus first harmonic, shown in Fig. 8. Harmonics higher than the fundamental are more important in the first normal stress difference, $N_1 = \tau_{xx} - \tau_{yy}$, and the strain rate. The third harmonic generation is revealed in the features with shorter wavelengths in the envelopes.

for the Giesekus model. The second difference in the profiles shown in Fig. 6b is more subtle and relates to the degree of nonlinearity or how the periodic curve departs from a single sinusoidal form. This second feature is more evident when the distribution of the Fourier coefficients across the gap is investigated, as we do next.

Harmonic analysis of the shear stress time series is carried out using Eq. (19) to calculate their Fourier coefficients, $a_i(y)$ and $b_i(y)$. In addition, the corresponding harmonic amplitudes are calculated as $I_i = \sqrt{a_i^2 + b_i^2}$. In the intermediate-gap regime, spatial variation of the harmonics become important in the analysis of the results. In particular, as it will be discussed in Section 5.1.2, we use spatial symmetry of the fundamental harmonic to determine resonance heights. Fig. 7a shows the spatial dependence of the resulting first harmonic amplitude, I_1, for the UCM model and gap heights:

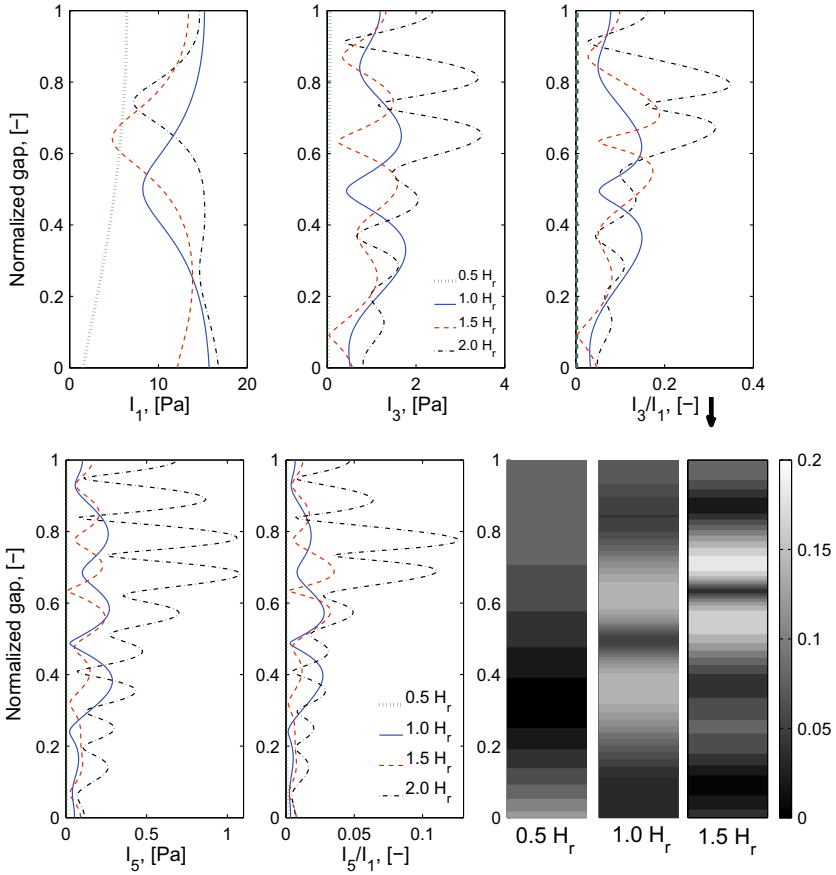

Fig. 10. Contributions of the first, third, and fifth harmonics for the Giesekus shear stress for gap heights that are multiples of the resonance height, $H_r^G = 4.4$ cm. Note also that the fifth harmonic is not always negligible, adding an additional level of nonlinearity in the analysis of the material response. Sweeps across the gap, with I_3/I_1 as the metric for nonlinearity. Grayscale curves representing the distribution of nonlinear behavior across the gap. Interlacing of dark and light layers convey interlacing layers of linear and nonlinear behavior within the gap.

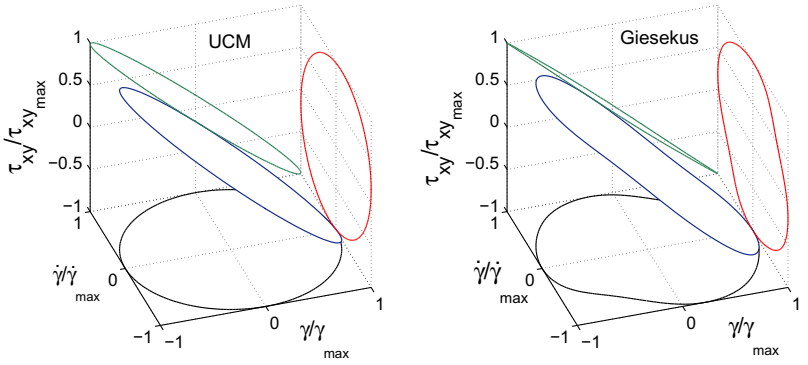

Fig. 11. Three-dimensional Lissajous–Bowditch parametric curves, $(\gamma(t), \dot{\gamma}(t), \tau_{xy}(t))$, corresponding to data in the middle of the gap for the UCM model (left) and the Giesekus model (right). The basis of the LAOS analysis in the gap-loading limit is a circle in the base plane $\gamma - \dot{\gamma}$. These figures show that for the Giesekus fluid this condition no longer holds in the intermediate gap height regime. Here $\eta_0 = 10$ Pa s, $\lambda = 1$ s, and $\alpha_g = 0.35$ for the Giesekus model.

$H = 0.5H_r$, H_r, $1.5H_r$, $2H_r$. Recall that in the UCM model, harmonics higher than the fundamental are negligible after initial transients have passed. The feature of interest in that figure is the non-monotonic dependence of $\max_y(I_1(y))$ as the gap height ranges from half-integer to integer multiples of the resonant height, in agreement with [5]. To amplify this behavior, in Fig. 7b, we vary the gap height continuously, and compute $\max(I_1(y))$, which can arise anywhere in the gap and not necessarily at the driving plate; for more details on this behavior see [5]. As hinted by Fig. 7a the amplitude of the stress response can be intensified by being in and out of resonance, which has important consequences in the nonlinear behavior studied next.

5.1.2. A criterion for nonlinear resonance heights for non-constant wave speeds

Following the results shown in Fig. 7, we want to investigate the effects of the gap height on the Giesekus model to explore the coupling between resonance height and nonlinearity. Recall that our estimate of the resonance length comes from the linear assumption $\tau_{yy} = 0$ in Eq. (13). However, for the quasi-steady solutions of

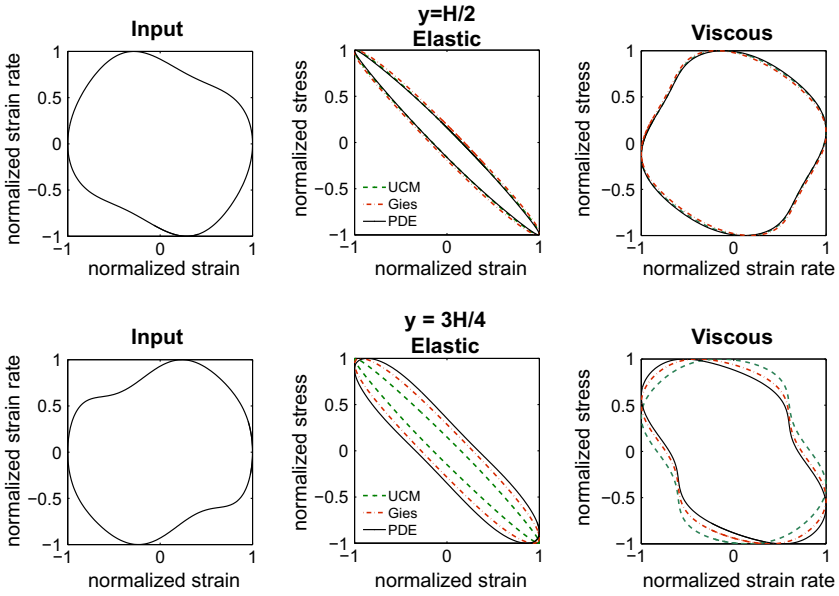

Fig. 12. This figure compares results from three types of simulations: solutions in the intermediate-gap regime for the Giesekus model-denoted PDE (solid lines), UCM model in the gap-loading limit with a nonlinear strain rate input (dashed lines) and Giesekus model in the gap-loading limit with a nonlinear input (dot-dashed lines). Nonlinearity can be quantified by differences between the three types of simulations. In the gap-loading limit, difference between UCM and Giesekus represent *local* departures from linear behavior. Differences between the Giesekus and PDE curves show spatial contributions to the nonlinear behavior. In the middle of the gap, these contributions are minimal indicating a local linear response. For $y = 3H/4$, spatial contributions are not trivial demonstrated by the differences between the three curves.

the Giesekus model the corresponding resonant height not only differs from the linear resonant height, but the wave speed varies in space and time through $\tau_{yy}(t,y) \neq 0$. By analogy with the UCM resonant features, we estimate a resonance length by finding the gap height for which the minimum of the first harmonic of the shear stress is located exactly at the middle of the gap. This notion is based on intuition about constructive interference of counter-propagating waves at resonance when the top boundary is fixed. For $A/H = 0.5$ and $\omega = 2\pi$ rad/s, we find for Giesekus $H_r^G = 4.4$ cm, whereas for UCM $H_r^{UCM} = 5$ cm. The fact that $H_r^G < H_r^{UCM}$ is due to the nonzero normal stresses in the Giesekus fluid, which in turn results in a decrease of the wave speed. In fact we found that for the Giesekus model the wave speed, $c = \sqrt{(G_0 + \tau_{yy})/\rho}$, can have values within the gap that are three orders of magnitude smaller than the linear wave speed, $c_L = \sqrt{G_0/\rho}$.

5.1.3. Spatial distribution of nonlinear LAOS behavior

In this subsection we ask a simple question: if we filter the fundamental harmonics at each height in the gap to get the linear projection of the response, how does the nonlinearity in the Giesekus model alter this linear response structure? Fig. 8 shows the fundamental harmonic contribution, I_1, of the shear and normal stresses, strain and strain rate, and corresponding velocity and displacement for the UCM model (which has only the fundamental harmonic) and Giesekus model. The upshot of Fig. 8 is that nonlinearity has a significant global impact on the "linear" response structure. Next, Fig. 9 shows the full Giesekus response functions next to the linear first harmonic projections of Fig. 8. Clearly, the higher harmonic structure is responsible for greater amplitudes of each response feature, and for higher spatial wave numbers, as a consequence of frequency-dependent wavelengths. Note that the most significant difference between the first harmonic and full harmonic envelopes arise in first normal stress difference, N_1, and the rate of strain, $\dot{\gamma} = \partial v_x(y,t)/\partial y$. This observation is representative of all simulations and will influence our choice of metrics of nonlinearity. Since the rate of strain is "more nonlinear" than the shear stress, nonlinearity metrics should be based on fluidities and compliances, rather than moduli and viscosities, similar to stress-controlled experiments in the gap-loading limit [29].

Anticipating an experiment where passive tracers are tracked in time, we use Fourier analysis of each feature in Fig. 9 at each height in the gap. Fig. 10 shows the contributions of the first (I_1), third(I_3), and fifth (I_5) harmonics for the Giesekus shear stress for gap heights that are multiples of the resonance height, as well as the ratios I_3/I_1 and I_5/I_1 proposed as metrics of nonlinearity, as discussed in Section 4.2.1. The purpose of these plots is to investigate the effects of being in and out of the resonance height and to visualize interlacing layers of linear and nonlinear responses within the gap, shown in the final panels of Fig. 10. The spatial distribution of the layering and the degrees of nonlinearity are strongly affected by the gap height relative to the linear resonance height.

Another important feature of Fig. 10 is the asymmetric distribution of the nonlinear behavior across the gap. For example, when $H = 1.5H_r^G$ the third and fifth harmonics are smaller close to the driving plate and increase significantly as they approach the upper fixed plate. This means that close to the bottom plate, the shear stress is larger in response to a plate displacement amplitude that

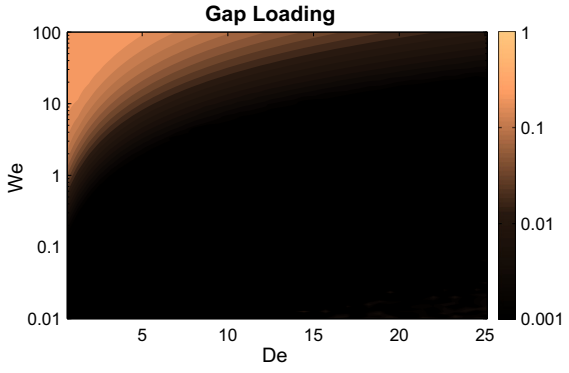

Fig. 13. I_3/I_1 for strain rate from simulations of the Giesekus model in the gap-loading limit.

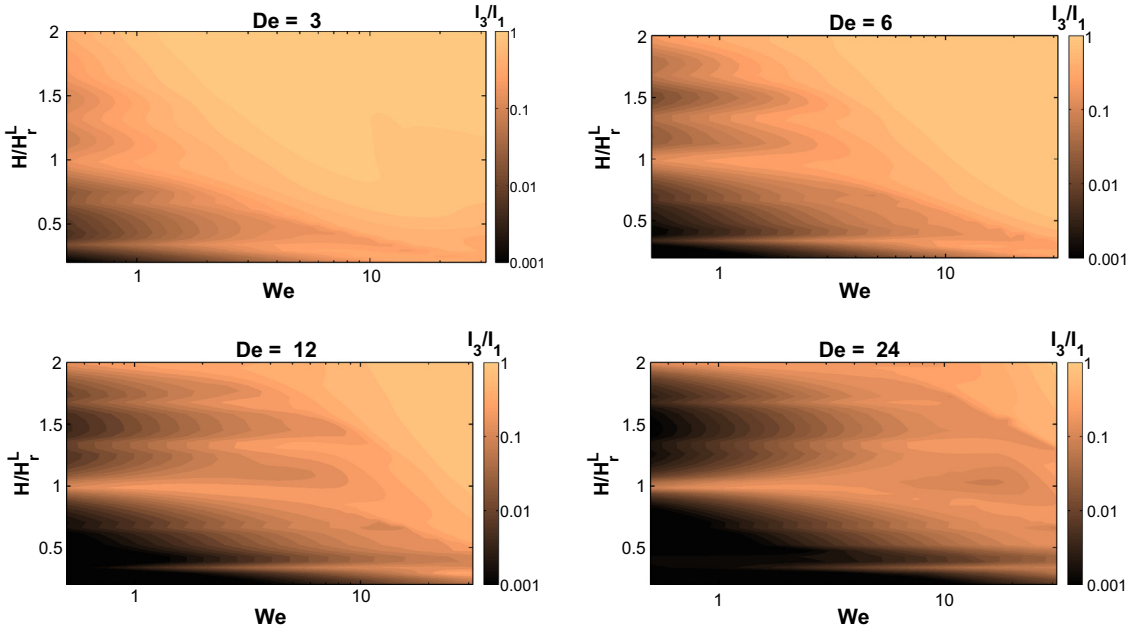

Fig. 14. Magnitude of $\max_y(I_3/I_1)$ of strain rate time series as a function of *De* and *We* numbers and gap height. Similarly to the gap-loading regime, increasing *De* results in a reduction of the nonlinear behavior. However, unlike the gap-loading regime, in the intermediate regime nonlinearities remain for large *De*, especially at multiples of the resonance height.

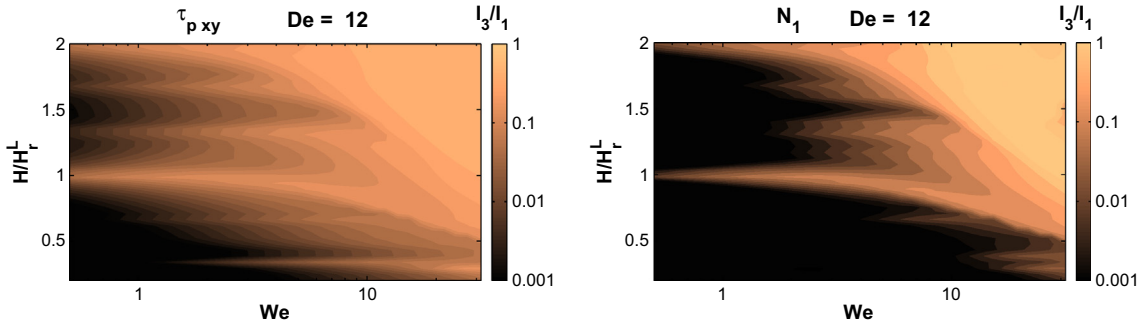

Fig. 15. $\max_y(I_3/I_1)$ for shear stress and first normal stress difference for zero velocity boundary condition. Note the light band at $H/H_r^L = 1$ for $We \ll 1$ and how it deviates from this value as *We* increases, indicating that the resonance length decreases with increasing *We* number.

is three times larger, recall $A/H = 0.5$ is held fixed in all simulations. Yet the local response near the plate shows no higher harmonic generation, indicating a linear behavior. On the other hand, in the top half of the gap, the third and fifth harmonics are larger indicating an increase in the nonlinear behavior of the shear stress. These observations strengthen our previous claim that measurements of stress at either boundary are insufficient to detect interior nonlinear response in this heterogeneous limit.

The consequences of this asymmetrical distribution of layers of linear and nonlinear response will be explored elsewhere, and hereafter, we focus our attention at the resonance height were the symmetry with respect to the middle of the gap is conserved.

5.2. Lissajous–Bowditch curves in the intermediate-gap regime

Another metric of nonlinear LAOS behavior of viscoelastic materials is the projection of model solutions onto Lissajous–Bowditch curves. A three-dimensional Lissajous–Bowditch plot is a parametric curve of the form $(\gamma(t,y_i), \dot{\gamma}(t,y_i), \tau_{xy}(t,y_i))$, where y_i is some height within the gap. Elastic Lissajous–Bowditch curves are projections onto the $\tau_{xy} - \gamma$ plane, and viscous Lissajous–Bowditch curves are projections onto the $\tau_{xy} - \dot{\gamma}$ plane. It is straightforward to show that for linear viscoelasticity, each of these planar projections is constrained to lie on an ellipse. Deviations of either the viscous or elastic Lissajous curves from an ellipse are indications of nonlinear behavior. *Here we highlight the fact that this metric of nonlinearity relies on the assumption that the parametric curve* $(\gamma(t), \dot{\gamma}(t))$ *is always a circle, which is only guaranteed in the gap-loading limit*. However, in the intermediate-gap regime, this constraint is violated for a nonlinear constitutive behavior (like the Giesekus model) everywhere except at the boundaries.

As an illustration, in Fig. 11 we plot 3D Lissajous–Bowditch curves from numerical simulations of the UCM and Giesekus models, extracting data in the middle of the gap, $y = H/2$, when $H = H_r$. Since for the UCM model higher harmonics than the fundamental are negligible at all points within the gap, projections of the Lissajous–Bowditch curve onto the $\gamma - \dot{\gamma}$ plane are always circles.

In stark contrast, *all* projections (i.e., including γ, $\dot{\gamma}$!) of the 3D Lissajous–Bowditch curves for the Giesekus model away from the plates may be non-elliptical; higher harmonics even in the strain and strain rate are possibly non-zero, as demonstrated by Fig. 9.

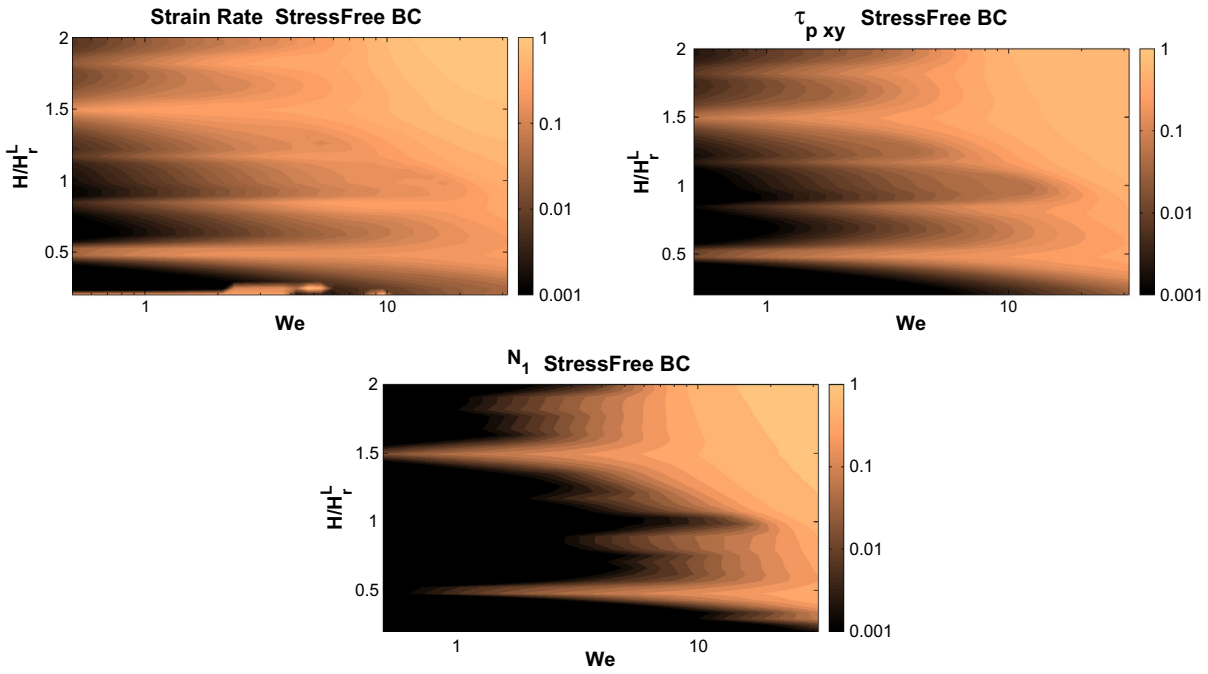

Fig. 16. $\mathrm{Max}_y(I_3/I_1)$ for shear stress and first normal stress difference with zero stress boundary conditions. Shifting in the nonlinear peaks away from $H/H_r^L = 1$ shows that the properties of the reflecting wave, i.e., amplitude and phase, are critical in the distribution of nonlinear behavior within the gap.

That is, it is not possible to obtain a 2D circular projection of the 3D Lissajous–Bowditch curve, the basic assumption of this LAOS metric in the gap-loading limit. *This implies that one can no longer define metrics of nonlinearity based on deviations from elliptical shapes.* These fundamental differences between the usual LAOS analysis in the gap-loading limit and our studies of heterogeneous behavior call for new measures of nonlinearity. In the following subsections we analyze the consequences of this observation.

5.2.1. Gap-loading results with a nonlinear input

In the gap-loading regime, where the Lissajous–Bowditch curve in the base plane $(\gamma - \dot{\gamma})$ is a circle, characterization of the nonlinear behavior is based on the explicit mapping from this circular curve to stress projections onto the $\gamma - \tau_{xy}$ and $\dot{\gamma} - \tau_{xy}$ planes. Here we are interested in whether the Lissajous–Bowditch curves at any gap height in the full PDE simulation can be inferred from the time series of $\gamma - \dot{\gamma}$ at that gap height. This is a subtle question: the answer will be yes only if there is no spatial coupling in the global response across the gap. Since we have physical boundary conditions at the plates, we fully expect the answer to be no. The point of this illustration, however, is that one cannot draw significant inferences about local material response from monitoring of the local $\gamma - \dot{\gamma}$ time series when the response is nonlinear.

Before giving the Giesekus results, we first show that one can indeed employ a local viscoelastic inference at any gap height for the UCM model. We consider the gap-loading limit first, for which the UCM model is exactly solvable for an arbitrary imposed Fourier series for the strain rate of the form,

$$\dot{\gamma}(\omega, t) = \sum_{\text{n:odd}} A_n \sin(n\omega t) + B_n \cos(n\omega t).$$

The UCM stress is given by,

$$\tau_{xy}(\omega, t) = \sum_{\text{n:odd}} G_n'(\omega) \sin(n\omega t) + G_n''(\omega) \cos(n\omega t),$$

where the corresponding Fourier coefficients are given explicitly,

$$G_n'(\omega) = \frac{A_n + (n\omega)B_n}{1 + (n\omega)^2}, \quad G_n''(\omega) = \frac{B_n - (n\omega)A_n}{1 + (n\omega)^2}. \tag{20}$$

These results are shown in Fig. 12 as projections of the 3D Lissajous–Bowditch curves. In this case, the curves for the UCM model are no longer ellipses, as higher harmonics are communicated to the stress from the nonlinear imposed strain rate, as dictated by Eq. (20). Results for the Giesekus model in the gap-loading limit with a nonlinear input are also shown in dot-dashed lines. In the middle of the gap, $y = H/2$, and since the differences between Giesekus and UCM are negligible, it is implied that for the locally imposed nonlinear strain rate, the stress response is linear. On the other hand, results for $y = 3H/4$ indicate that, *locally*, the stress from the Giesekus model is behaving nonlinearly, revealing the non-trivial influences of spatial heterogeneity in the local response.

The comparison between the heterogeneous Giesekus response and this artificial simulation in the gap-loading limit reveals the influence of nonlocal spatial structure, i.e., heterogeneity. That is, one simulation is a chain of uncoupled stress tensorial ODEs, and the heterogenous Giesekus simulation can be viewed as a spatially coupled chain of tensorial ODEs. Again, the point of this illustration is simply that one cannot use local time series of $\gamma - \dot{\gamma}$ inside the gap to infer material consequences of nonlinearity.

5.3. Pipkin diagrams in the intermediate-gap regime

In this section, we study the effects of varying the Weissenberg and Deborah numbers on the material response in the intermediate-gap regime. In the gap-loading limit, it is typical to represent viscoelastic phenomena in the parameter plane of $We = \lambda U_0/H$ and $De = \lambda\omega$, creating what is called a Pipkin diagram [18]. This is to be expected since an experiment in the gap-loading limit can only control conditions at the driving plate, i.e., frequency and amplitude. In contrast, in the intermediate-gap height regime the response depends not only on the driving conditions and material properties, but also on the height of the gap, as shown in previous sections. A 2D Pipkin diagram is insufficient to characterize

material response, so we append another axis (gap height) to represent often dramatic differences in material responses.

5.3.1. Pipkin diagram: Dirichlet boundary conditions for velocity

Fig. 13 plots contour levels representing the magnitude of I_3/I_1 for the strain rate in the gap-loading limit. It is clear from that figure that nonlinear behavior (bright spots in the figure) in the gap-loading limit requires larger *We* compared to intermediate gap. This difference stems from the fact that in the gap loading-limit there is no formation of structures, so that the maximum strain amplitude is always at the imposed plate. On the other hand, in previous sections we show that in the intermediate-gap regime the maximum strain amplitude can arise anywhere in the gap. This implies that amplitudes in the interior of the gap can be large enough to result in a nonlinear behavior of the fluid, even though the given *We* number is not large enough to induce nonlinearity close to the driving plate.

We explore this behavior in the intermediate-gap height regime in Fig. 14 by comparing contour plots of $\max_y(I_3/I_1)$ in *We* number and *H* for different values of *De* number. The first observation is that as *De* number increases, larger gap heights and *We* numbers are necessary to induce nonlinear behavior. On the other hand, the common feature of these plots is the 'peak' in the nonlinear behavior when the gap height is comparable to the value of the linear resonance height, i.e., $H \simeq H_r^L$ as $We \to 1$. This peak is more pronounced for higher *De* number, since the nonlinear behavior out of resonance is diminished as the high frequency reduces formation of inhomogeneities. Furthermore, 'peaks' and 'valleys' in the contour plots show that linear and nonlinear material responses, for fixed *We*, can be attained by being in and out of resonance.

In Fig. 15 we plot the Pipkin diagrams, corresponding to $De = 12$, of the shear stress, $\tau_{p\ xy}$, and the first normal stress difference, $N_1 = \tau_{p\ xx} - \tau_{p\ yy}$. Note that higher harmonics in N_1 for $We = O(1)$ appear only at resonance. In addition, from these figures one can clearly observe the decrease of the resonance height as function of the *We* number. That is, for small *We* numbers the peak in the contour plot with respect to H/H_r^L plateaus at one, and as *We* increases the location of the peak with respect to *H* decreases. This in agreement with our discussion in Section 5.1.2, and the fact that normal stress generation, $\tau_{p\ yy}$, reduces the wave speed.

5.3.2. Pipkin diagram: Dirichlet boundary conditions for shear stress

In an experiment like the cell culture discussed in the introduction, the top boundary conditions are no longer vanishing velocity, but rather there is a zero stress (stress-free) condition at the mucus-air interface. Fig. 16 shows the resulting Pipkin diagrams under these conditions for the strain rate, the shear rate, and the first normal stress difference with $De = 12$. These figures indicate that the nature of the reflected waves affects the location and magnitude of nonlinear layers within the gap, stressing our previous claim that nonlinearities within the gap arise from constructive and destructive interference of counter-propagating waves and the importance of the given boundary conditions.

6. Conclusions

We have employed numerical simulations of the UCM and Giesekus constitutive models coupled to the momentum balance equations to explore heterogeneity in finite, uniform thickness viscoelastic layers with oscillatory shear driving conditions. In particular, we explore intermediate gap heights between the gap-loading and the surface-loading limits. Gap heights in this regime allow the reflection and superposition of counter propagating traveling shear waves within the layer.

In this intermediate gap regime of heterogeneous phasic shear, metrics of nonlinearity developed for the gap-loading limit, and described in Section 4.2.1, are no longer applicable. Nonlinear behavior in the heterogeneous limit is characterized by the presence of harmonics higher than the fundamental in all viscoelastic features, i.e., shear stress, strain rate, and strain. The fact that not a single feature is linear in the intermediate regime, precludes the use of such "non-parametric" (i.e., model independent) metrics. Therefore, to explore, detect, and assess nonlinearity in the heterogeneous shear regime, one must abandon non-parametric metrics and a high premium is then placed on models and simulations. The present study therefore selects a canonical nonlinear constitutive equation (Giesekus) and reports on the phenomena that arise in phasic shear, organizing the wide range of behavior in generalized Pipkin diagrams.

A rich array of nonlinear behavior, highlighted by interlacing layers of linear and nonlinear response, is revealed by extensive simulations of linear and nonlinear coupled systems of PDEs. The nonlinear response is intensified by gap heights that are multiples of the resonance height determined by the characteristic speeds of the propagating shear and stress waves, $c = \sqrt{(G_0 + \tau_{yy})/\rho}$. For the Giesekus constitutive equation we track the resonance height dependence and corresponding features versus driving conditions and material properties, captured by the spatial dependence of the normal stress in the direction of the flow gradient, τ_{yy}. We find that nonlinear behavior can be suppressed by selecting heights out of resonance, while maintaining the same driving conditions and material parameters, i.e., *We* and *De* numbers.

As motivated in the Introduction, the parallel plate geometry was chosen to explore heterogeneous nonlinear responses in a sheared viscoelastic layer out of convenience: the governing system of quasilinear partial differential equations reduces to one space dimension. Future challenges lie in extending these studies to geometries of lung tissue cell cultures and to lung airways, where at least two space dimensions are needed.

Acknowledgments

This work originated with and has benefited from discussions with colleagues involved in the University of North Carolina *Virtual Lung Project*. The research effort was sponsored by NSF DMR-1122483, DMS-1100281, AFOSR FA9550-12-1-0178. The authors wish to thank S. Mitran for the generosity of his numerical software [http://mitran.web.unc.edu].

References

[1] F. Adler, W. Sawyer, J. Ferry, Propagation of transverse waves in viscoelastic media, J. Appl. Phys. 20 (1949) 1036–1041.
[2] J. Ferry, Viscoelastic Properties of Polymers, John Wiley and Sons, 1980.
[3] S. Mitran, M. Forest, L. Yao, B. Lindley, D. Hill, Extensions of the ferry shear wave model for active linear and nonlinear microrheology, J. Non-Newtonian Fluid Mech. 154 (2008) 120–135.
[4] B. Lindley, E. Howell, B. Smith, G. Rubinstein, M. Forest, S. Mitran, D. Hill, R. Superfine, Stress communication and filtering of viscoelastic layers in oscillatory shear, J. Non-Newtonian Fluid Mech. 156 (2009) 112–120.
[5] B. Lindley, M. Forest, B. Smith, S. Mitran, D. Hill, Spatial stress and strain distributions of viscoelastic layers in oscillatory shear, Math. Comput. Simul. (2010).
[6] N. Balmforth, Y. Forterre, O. Pouliquen, The viscoplastic stokes layer, J. Non-Newtonian Fluid Mech. 158 (2009) 46–53.
[7] D. Hill, B. Button, Establishment of respiratory Air-Liquid interface cultures and their use in studying mucin production, secretion, and function, in: D.J. Thornton (Ed.), Mucins, Springer, 2012.
[8] K. Cho, K. Hyun, K. Ahn, S. Lee, A geometrical interpretation of large amplitude oscillatory shear response, J. Rheol. 49 (2005) 747–758.
[9] R. Ewoldt, A. Hosoi, G. McKinley, New measures for characterizing nonlinear viscoelasticity in large amplitude oscillatory shear, J. Rheol. 52 (2008) 1427–1458.
[10] S. Rogers, B. Erwin, D. Vlassopoulos, M. Cloitre, A sequence of physical processes determined and quantified in LAOS: application to a yield stress fluid, J. Rheol. 55 (2011) 435–458.

[11] J. Schrag, Deviation of velocity gradient profiles from the gap loading and surface loading limits in dynamic simple shear experiments, J. Rheol. 21 (1977) 399–413.
[12] H. Sim, K. Ahn, S. Lee, Large amplitude oscillatory shear behavior of complex fluids investigated by a network model: a guideline for classification, J. Non-Newtonian Fluid Mech. 112 (2003) 237–250.
[13] A. Gurnon, N. Wagner, Large amplitude oscillatory shear (LAOS) measurements to obtain constitutive equation model parameters: Giesekus model of banding and nonbanding wormlike micelles, J. Rheol. 56 (2012) 333–351.
[14] H. Winet, G. Yates, T. Wu, J. Head, On the mechanics of mucociliary flows III. Flow-velocity profiles in frog palate mucus, J. Appl. Physiol 56 (1984) 785–794.
[15] H. Giesekus, A simple constitutive equation for polymer fluids based on the concept of deformation–dependent tensorial mobility, J. Non-Newtonian Fluid Mech. 11 (1982) 69–109.
[16] R. Bird, C. Curtiss, R. Armstrong, O. Hassager, Dynamics of Polymeric Liquids: Fluid mechanics, Wiley, 1987.
[17] R. Larson, Constitutive Equations for Polymer Melts and Solutions, Butterworth, 1988.
[18] A. Pipkin, Lectures on Viscoelastic Theory, Springer-Verlag, New York, 1972.
[19] L. Casanellas, J. Ortín, Laminar oscillatory flow of Maxwell and Oldroyd-B fluids: theoretical analysis, J. Non-Newtonian Fluid Mech. 166 (2011) 1315–1326.
[20] J. Adams, P. Olmsted, Nonmonotonic models are not necessary to obtain shear banding phenomena in entangled polymer solutions, Phys. Rev. Lett. 102 (2009) 067801:1–067801:4.
[21] L. Zhou, L. Cook, G. McKinley, Probing shear-banding transitions of the VCM model for entangled wormlike micellar solutions using large amplitude oscillatory shear (LAOS) deformations, J. Non-Newtonian Fluid Mech. 165 (2010) 1462–1472.
[22] K. Hyun, M. Wilhelm, C. Klein, K. Cho, J. Nam, K. Ahn, S. Lee, R. Ewoldt, G. McKinley, A review of nonlinear oscillatory shear tests: analysis and application of large amplitude oscillatory shear (LAOS), Prog. Polym. Sci. 36 (2011) 1697–1753.
[23] W. Philippoff, Vibrational measurements with large amplitudes, J. Rheol. 10 (1966) 317–334.
[24] S. Onogi, Non-Linear behavior of viscoelastic materials. I. Disperse systems of polystyrene solution and carbon black, J. Rheol. 14 (1970) 275–294.
[25] M. Wilhelm, Fourier transform rheology, Macromol. Mater. Eng. 287 (2002) 83–105.
[26] W. Yu, P. Wang, C. Zhou, General stress decomposition in nonlinear oscillatory shear flow, J. Rheol. 53 (2009) 215–238.
[27] K. Hyun, M. Wilhelm, Establishing a new mechanical nonlinear coefficient Q from FT-rheology: first investigation of entangled linear and comb polymer model systems, Macromolecules 42 (2009) 411–422.
[28] J.A. Giacomin, J. Dealy, Large-Amplitude Oscillatory Shear, Techniques in Rheological Measurement, London, Elsevier Applied Science, 1993.
[29] J. Läuger, H. Stettin, Differences between stress and strain control in the non-linear behavior of complex fluids, Rheol. Acta 49 (2010) 909–930.
[30] K. Atalik, R. Keunings, On the occurrence of even harmonics in the shear stress response of viscoelastic fluids in large amplitude oscillatory shear, J. Non-Newtonian Fluid Mech. 122 (2004) 107–116.